

A Comparison of the Use of Ultrasonic Melt Treatment and Mechanical Vibration in the Manufacture of Al5Si5Zn Alloy Feedstock for Thixoforming



C.T.W. PRONI, G.L. BROLLO, and E.J. ZOQUI 

The use of physical agents when casting aluminum alloys has proven to be an effective route for grain refinement and avoids the inconvenience of residual impurities left in the material when chemical agents are used. The application of ultrasonic waves to the molten metal before casting generates acoustic cavitation, which promotes extensive heterogeneous nucleation and contributes to degassing of the metal. In addition, the application of mechanical vibration during solidification has been proven to promote dendrite fragmentation, and therefore, grain refinement. The aim of this work is to evaluate microstructural refinement due to cavitation produced by ultrasonic melt treatment (UST) of Al5Si5Zn alloy (Al-5wt pctSi-5wt pctZn) and to compare the resulting microstructure with that achieved with and without simple mechanical vibration (MV) during casting so that the best manufacturing procedure for refining aluminum silicon feedstock for subsequent thixoforming can be identified. After casting, the alloy produced under each condition was partially melted to a 0.45 solid fraction to obtain a primary phase with a spheroidized microstructure. The rheological behavior of each semisolid slurry was also evaluated. Microstructural characterization was performed using optical and scanning electron microscopy. Mechanical performance was evaluated by means of tensile tests and hardness measurements. The use of ultrasonic stirring for 30 seconds resulted in slightly better mechanical performance than the other casting conditions. However, because of the short life expectancy of the sonotrodes, mechanical vibration can be considered a simpler, superior solution for feedstock production.

<https://doi.org/10.1007/s11663-019-01741-7>

© The Minerals, Metals & Materials Society and ASM International 2019

I. INTRODUCTION

THE efficiency of semisolid material (SSM) processing depends on adequate control of the solid-liquid transition and the semisolid slurry microstructure.^[1,2] In fact, the “*sensitivity of the liquid fraction, df_L/dT , at the desired liquid fraction, f_L , exclusively for the primary phase must be as low as possible*”.^[3–6] Solid particles in the primary phase in the eutectic liquid must be refined (maximum grain size 150 μm), homogeneously distributed and highly globular (*i.e.*, as round as possible)

and contain a limited amount of melted eutectic entrapped in their interior.^[7,8] When these conditions are met, the semisolid slurry will exhibit the thixotropic rheological behavior required for SSM processing (rheocasting or thixoforming).^[1–4]

Control of the solid-liquid transition depends almost exclusively upon the chemical composition of the material but is also affected by its morphology, which can be improved by chemical or physical refinement. Many industries use chemical agents for grain refinement and to improve spheroidization. However, only a fraction of the grain refiner truly acts as nucleation sites, and the other fraction remains as impurities in the alloy (mainly TiB_2), acting as potential sources of crack initiation under cyclical stress and leading to inferior mechanical performance. To overcome this limitation, the use of physical agents is suggested for grain refinement. Examples include cooling of the ingot mold during casting,^[9] mechanical stirring of the ingot during casting^[10,11] and application of ultrasonic cavitation in the molten metal before casting.^[12,13]

C.T.W. PRONI, G.L. BROLLO, and E.J. ZOQUI are with the Materials and Manufacturing Department, School of Mechanical Engineering, University of Campinas UNICAMP, R. Mendelév, n. 200, Campinas, SP, 13083-860, Brazil. Contact e-mail: zoqui@fem.unicamp.br

Manuscript submitted April 17, 2019.

Article published online December 2, 2019.

It is well known that grain size is inversely proportional to the square root of the energy transfer rate. Hence, the higher the cooling rate, the smaller the grain, or, in other words, as the cooling rate is reduced so the grain size increases. Because the cooling rate decreases toward the center, cast parts tend to have a finer grain near the outside.^[9] When applied during solidification, mechanical vibration (MV) increases dendrite fragmentation in the solidification front, and the new nuclei thus formed create small grains inside the ingot or cast part.^[10,11] MV also leads to gas bubbles being dragged to the surface of the molten metal, decreasing the porosity of the solidified metal, and generates convective flow in the liquid, causing fewer voids to form because of the metal contracts as it solidifies. Furthermore, the convective flow produced by MV enables newly formed crystals in the chill zone to detach and become distributed in the liquid metal.^[11]

Ultrasonic waves are formed by alternate expansion and compression cycles. When ultrasound is applied to a liquid, the compression cycles exercise a positive pressure on the molten mass, while expansion cycles create a negative pressure. This alternating effect produces high-intensity shock waves, called acoustic cavitation, which create micro-fluxes in the liquid.^[14] If the intensity of the ultrasonic vibrations is sufficiently high, cavitation can encourage extensive heterogeneous nucleation in the molten metal as a result of either the generation of nucleation sites when bubbles collapse or surface wetting of eventual impurities in suspension in the liquid, stimulating the growth of equiaxial crystals throughout the metal.^[12] If casting is carried out just after nucleation, the majority of the nuclei will remain stable.^[13] Furthermore, shock waves help to create other nuclei by fragmenting interdendritic arms^[14] and generate convective flow, which ensures that stable nuclei are distributed throughout the liquid.

In parallel, microbubbles generated by cavitation absorb a large proportion of the gasses (mainly hydrogen) dissolved in the molten metal. These bubbles are dragged to the surface of the liquid, leading to improved degassing.^[15,16] As a secondary effect, impurities such as oxides can also be dragged with the bubbles. Reducing porosity is a major challenge when processing cast aluminum alloys because the high reactivity of aluminum with hydrogen in the presence of humidity during casting and the production of raw material leads to substantial absorption of hydrogen by the liquid aluminum, resulting in pores in the solidified metal.

If the benefits of acoustic cavitation for grain refinement are to be achieved, the temperature of the liquid must be carefully chosen: it must be sufficiently high to ensure enough fluidity for bubble displacement but not so high that the newly formed nuclei melt.^[13] Thus, if the processing parameters are adequately chosen, the use of ultrasound in the liquid metal will ensure that a refined, homogeneous, partially degassed microstructure is achieved, leading to improved mechanical behavior of the cast alloy.

A previous paper by our research group showed that Al-5wt pctSi-5wt pctZn alloy (or Al5Si5Zn) has suitable thermodynamic characteristics for semisolid processing. It has a wide semisolid processing window, from

566.6 to 615.2 °C, within which the liquid fraction varies from 45 to 100 pct and the liquid-fraction sensitivity is always lower than the recommended value of 0.03 °C⁻¹.^[17] Refining the microstructure of this alloy is, therefore, key to producing suitable feedstock for thixoforming. To evaluate the effects of different physical refinement techniques that could be used to this end, three processing conditions were tested: simple casting in a cooled copper mold (AC), casting under mechanical vibration (MV) and casting after ultrasound melt treatment (UST).

II. EXPERIMENTAL PROCEDURE

The alloy was melted in a conventional furnace and poured at 70 °C above the liquidus into a cooled copper mold (30 mm D × 220 mm L). The flow rate of the cooling water was 15 L/min. This procedure corresponds to the AC condition referred to in the previous section and was also used for the other conditions. For the MV condition, the alloy was mechanically vibrated as it solidified in the cooled mold using an eccentric shaft (mechanical hammer) with an amplitude of 0.7 mm, frequency of approximately 800 Hz and acceleration ranging from 1.59 to 2.46 ms⁻² to break up the dendritic solid as it formed. Finally, for the UST condition, a Sonitron ultrasound system (20 kHz, 2.8 kW, with a steel AISI 4340 sonotrode) was used with the tip of the sonotrode placed 5 mm under the surface of the molten metal in a volume (without any protective atmosphere) corresponding to a 0.5-kg ingot for 15, 30 and 60 seconds before pouring. After the UST, the casting was performed as described above. Figure 1 outlines the experimental procedure.

The chemical composition of the Al5Si5Zn alloy (Al-5wt pctSi-5wt pctZn) was determined with an Anacom BILL optical emission spectrometer and is shown in Table I (average ± standard deviation corresponding to four measurements). Thermo-Calc[®] simulation software was used to produce the liquid fraction vs temperature curve so that the target temperature for the semisolid characterization and processing could be

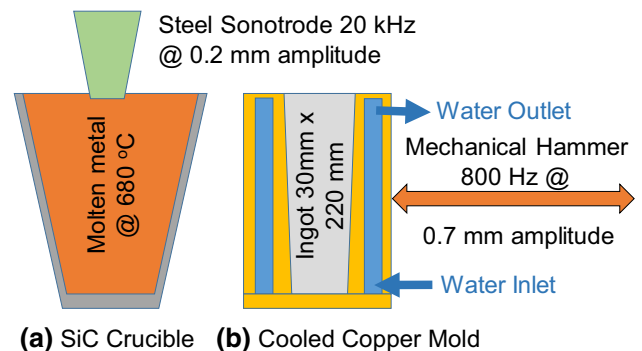


Fig. 1—Schematic of the experimental approach adopted showing (a) the SiC crucible and the sonotrode used for the UST before the molten metal was poured and (b) the cooled copper mold used to solidify the ingot with and without mechanical vibration (Color figure online).

Table I. Chemical Composition of the Al5Si5Zn Alloy (Average ± Standard Deviation in Weight Percent)

Element	Zn	Si	Fe	Mg	Cu	Mn	Al
Weight Percent ²	4.9 ± 0.3	5.5 ± 0.1	0.24 ± 0.02	0.197	0.117	0.082	bal ¹

¹Balance.²Unless otherwise indicated, maximum standard deviation is ± 0.005.

determined. The simulation returned a T_{Solidus} of 503 °C, T_{Liquidus} of 618 °C and T_{Knee} (the temperature above which all the eutectic should be liquid) of 566.6 °C, indicating a suitable processing window between $T_{\text{SSMI}} = 566.6$ °C and $T_{\text{SSMF}} = 615.2$ °C. The target temperature chosen for processing was therefore $T_{\text{P}} = 588$ °C, at which the solid fraction of the mush alloy is expected to be 0.45.

Based on the Thermo-Calc[®] predictions, the alloy processed under each of the conditions tested was heated to 588 °C at 50 °C/min in an 8 kHz 20 kW Norax induction heating furnace and immediately water quenched to characterize its morphological evolution in the semisolid state.^[18]

Compression tests were performed for each condition using an instrumented compression rheometer.^[18] Thixoforming samples (30 mm D × 30 mm H) were taken from the as-cast billets and heated to the semisolid state in the same manner and under the same conditions as in the heat-treatment experiments. After the target temperature had been reached, an engineering strain of 0.8 was imposed at a strain rate of approximately 4.2 s⁻¹. The output data from the mechanical press were used to plot the engineering stress (σ in MPa) vs engineering strain (e) and apparent viscosity (μ in Pa.s) vs shear rate ($\dot{\gamma}$ in s⁻¹) curves based on the following equations^[7,8,18]:

$$e = 1 - \frac{h}{h_0} \quad [1]$$

$$\sigma = \frac{Fh_0}{V}(1 - e) = \frac{Fh}{V} \quad [2]$$

$$\dot{\gamma} = - \left(\frac{\sqrt{V}}{\pi} \right) \left(\frac{dh}{dt} \right) \frac{1}{2h^{2.5}} \quad [3]$$

$$\mu = - \frac{2\pi Fh^5}{3V^2 \left(\frac{dh}{dt} \right)} \quad [4]$$

where F is the load, h and h_0 are the instantaneous and initial heights of the sample, respectively, V is the constant volume of the sample and t is the time. The same compression rheometer was used until a strain of 0.4–0.5 was reached.

Specimens for the tensile tests were taken from a 70-mm-long segment of the ingots and thixoforged in an open die. Tensile tests were performed in a universal testing machine (MTS, model 810, 100 kN capacity load cell) connected to a Test Star II system with an initial

velocity of 1.2 mm/min. The specimens were machined in accordance with the ASTM E8M-16a standard^[19] (6.0 ± 0.1 mm D, 30 mm A, 6 mm R, 24.0 ± 0.1 mm G). The yield stress was calculated using a 0.2 pct offset. Six specimens were tested for each processing condition (AC, MV and UST). Vickers hardness measurements were performed in a Future Tech FV-800 hardness tester using a 1 kgf load applied for 10 seconds to the base of those specimens used in the tensile tests for which the results were near the averages for each processing condition. Ten indentations were performed in each specimen.

The microstructures for the three conditions (AC, MV and UST) before heat treatment, after heat treatment and after thixoforming were characterized by conventional black and white (B&W) and polarized-light color microscopy using a Leica DM ILM optical microscope (OM—Leica Microsystems). For color microscopy, the samples were etched electrolytically in 1.8 pct Barker solution at 27 V for 180 seconds under stirring. Polarizing filters were used to obtain color images of the grains so that grains with the same crystal orientation had similar colorings. Observations were performed in the longitudinal direction of the ingots. Each primary phase observed separately in a conventional B&W micrograph is referred to here as a “globule”. It is assumed that adjacent globules with the same coloring in a polarized optical micrograph have the same interconnected “skeleton” structure in three dimensions (3D). This structure is in turn represented by the grain observed in the two-dimensional (2D) images. A complete explanation of the relationship between grain and globule can be found in an earlier work.^[20]

Grain size (GS) and globule size (GLS) were determined using the Heyn intercept method (ASTM International E112-13^[21]). Shape factor (circularity, C) was calculated using Image-J[®] 1.40 g software (V1.40, National Institutes of Health) and the equation $C = (4\pi A)/P^2$, where A is the area and P the perimeter ($C = 1$: sphere; $C \rightarrow 0$: needle). Particles smaller than 10 μm were not considered in the calculation. The phases in the alloy were identified using scanning electron microscopy (SEM).

III. RESULTS AND DISCUSSION

A. Feedstock Characterization

Figure 2 shows polarized color OM images of the alloy and the corresponding conventional black & white (B&W) micrographs for the three casting conditions studied, *i.e.*, casting in a cooled copper mold (AC) (a, b), casting under mechanical vibration (MV) (c, d) and casting after application of ultrasound (UST) for 15

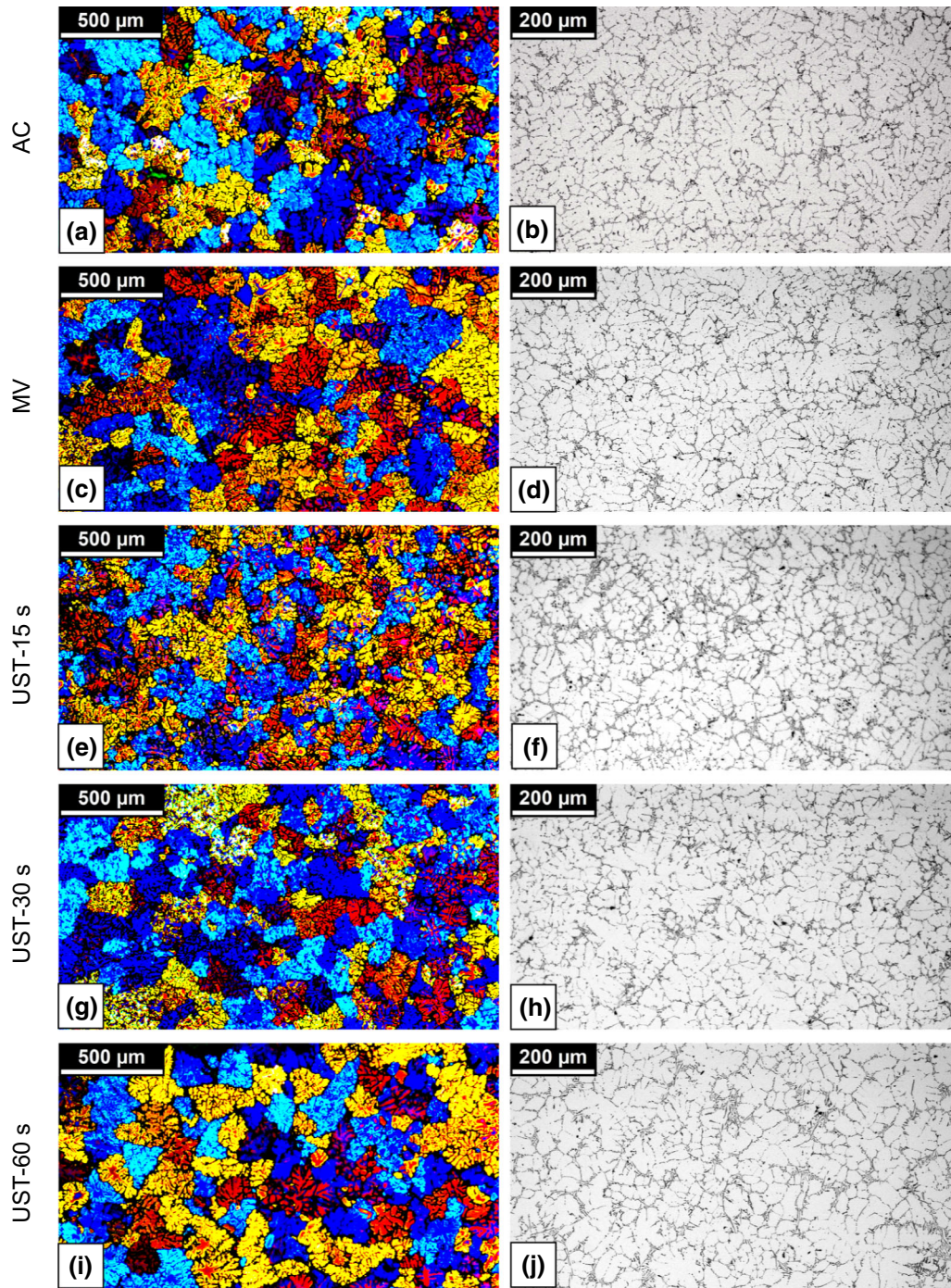


Fig. 2—OM images of the Al5Si5Zn alloy after casting for the three processing conditions studied: AC (*a, b*), MV (*c, d*) and UST-15s (*e, f*), UST-30s (*g, h*) and UST-60s (*i, j*) (Color figure online).

seconds (UST-15s in *e, f*), 30 s (UST-30s in *g, h*) and 60 seconds (UST-60s for *i, j*). The color images highlight the grains, while the B&W images highlight the dendrite arm spacing and the distribution of the eutectic phase between the arms.

For the as-cast conditions, there is a gradual reduction in the dendrite grain size from condition AC (coarser dendrites) through MV and UST-15s to UST-30s (more refined dendrites). This shows the

effectiveness in terms of grain refinement of the extensive nucleation promoted by ultrasound and the extensive fragmentation that occurred during mechanical vibration. However, for condition UST-60s, dendrite growth was observed, and the dendrites were similar in size to those found for condition MV. A probable explanation for this is that the long period in the liquid state resulted in melting of the nuclei that had formed.

Table II. Microstructural Parameters of the Feedstock Produced Under Conditions AC, MV and UST (Average \pm Standard Deviation)

Processing Condition	Grain Size (μm)	λ_2 (μm)	Porosity (Area Percent)
AC	170 \pm 29	35 \pm 7	1.6
MV	144 \pm 18	32 \pm 5	0.9
UST-15s	108 \pm 13	29 \pm 4	0.5
UST-30s	119 \pm 16	31 \pm 4	0.7
UST-60s	142 \pm 17	37 \pm 6	0.6

It should be noted that the microstructure seems to be more fragmented for condition UST-15s than for all the other conditions. For all the MV and UST samples, the microstructure is uniform along the entire radial section of the ingots, and there is a reduced or non-existent columnar zone. The conventional B&W micrographs do not show the extent and complexity of the grain but show the shape and size of the dendrite arms and the secondary arm spacing (λ_2). No significant differences can be observed between the various conditions tested, and the eutectic (secondary) phase is distributed homogeneously between the secondary arms for all the conditions. This phase, along with part of the primary α phase, will become liquid in the semisolid state, allowing spheroidization of the remaining solid, which is required for the forming process. Homogeneous distribution of this phase is essential for SSM processing. Table II shows the quantitative microstructural parameters measured for the conditions in Figure 2.

While grain size decreases by 15 pct from AC to MV and by 30 pct (average) from AC to UST, secondary arm spacing (λ_2) remains relatively stable. In fact, λ_2 is more sensitive to the cooling rate, which was the same for all the conditions tested. Porosity, which is measured as a percentage of the total area, was also affected by the treatment^[22] and decreased by 44 pct from AC to MV and by 62 pct from AC to UST (average). This is an important finding, as the feedstock will be used as raw material for thixoforming. The small amount of hydrogen present in cast aluminum alloys usually diffuses to the small pores in these alloys, causing them to become larger as the material is heated to the semisolid state and impairing the mechanical properties of the part produced. The lower the initial porosity (*i.e.*, the fewer and smaller the pores), the fewer the defects in the final product.

B. Morphological Characterization and Rheological Behavior

As presented in Section II, the alloy processed under each of the conditions tested was heated to 588 °C at 50 °C/min in an 8 kHz 20 kW Norax induction heating furnace and immediately water quenched to characterize its morphological evolution in the semisolid state. Rheological characterization was performed under the same heating conditions in a compression rheometer to determine the stress vs strain and apparent viscosity vs shear rate curves.

Figure 3 shows polarized color OM images of the alloy and the corresponding conventional B&W micrographs for the three casting conditions, AC (a, b), MV (c, d) and UST for 15 seconds (UST-15s, e, f), 30 seconds (UST-30s, g, h) and 60 seconds (UST-60s, i, j). As before, the color images highlight the grains, while the B&W images highlight the dendrite cell size or, in this particular case, the globule size and morphology.

As expected, all the conditions tested had a high degree of spheroidization, as shown by the grain in the color micrograph and the globule in the corresponding B&W micrograph. Heating to the semisolid state allows Ostwald ripening and coalescence to occur as a result of the reduction in the surface energy of the remaining solid particle. For all the conditions, several branches can be seen in the polarized color images, which, although separate, are the same color. These branches can be considered as one entity, *i.e.*, one grain, since they have the same orientation and may be interconnected in a 3D skeleton.^[11,17,18,20] Condition MV appears to have the greatest spheroidization and the most grains per unit area. In contrast, conditions AC and UST-60s have the least spheroidized grains because of the coarse initial microstructure.

Conventional B&W characterization shows the traditional semisolid structure of the globular primary α phase surrounded by the eutectic secondary phase with some entrapped liquid. This is in fact eutectic phase that was entrapped between two or more dendrite arms and remained inside the solid particle during coalescence. This is almost completely absent in the UST-30s sample.

Table 3 summarizes the quantitative data obtained after heating the feedstock to the semisolid state. In the AC and MV samples, the grains were smaller than in the original as-cast material, whereas in the UST samples they were slightly larger. This phenomenon has been explained in a previous paper^[23] and depends on the fragmentation of the structure and the creation of new grains even without any recrystallization phenomenon. It would seem, therefore, that the UST samples already have the most refined structure possible. The globule size, which can be measured in the B&W micrograph, is larger for the AC and MV samples and slightly smaller for the UST samples, especially for the condition UST-30s. The degree of spheroidization, measured by the circularity shape factor, was highest for the MV samples. The UST-60s sample had the lowest circularity because of the coarser structure mentioned.

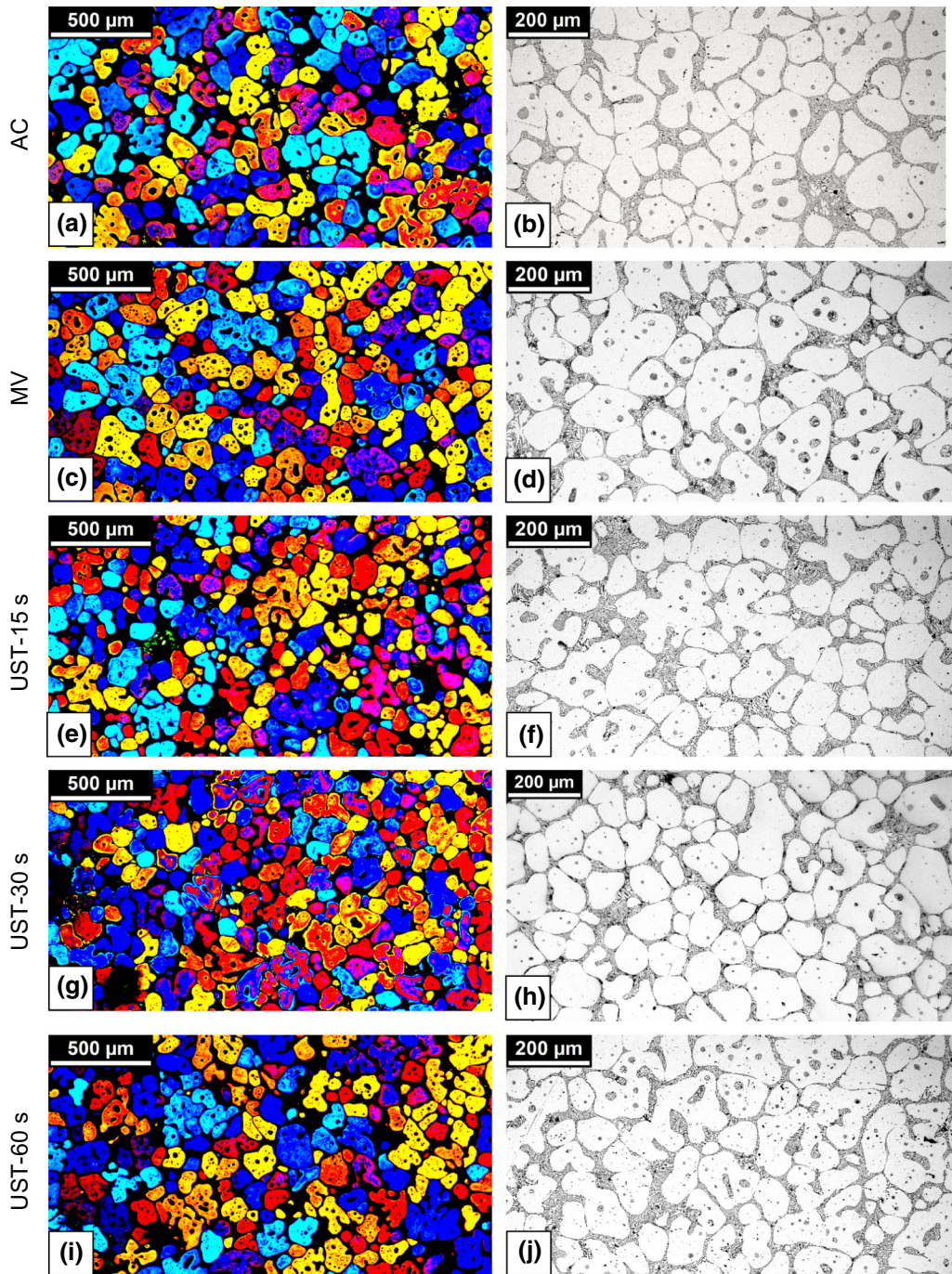


Fig. 3—OM images of the Al5Si5Zn alloy after partial melting at 50 °C/min to 588 °C followed by water quenching for the three processing conditions studied: AC (a, b), MV (c, d) and UST-15s (e, f), UST-30s (g, h) and UST-60s (i, j) (Color figure online).

As expected, the porosity increases because of the migration of H^+ into small pores, which become larger but more globular in shape. While on the one hand, the porosity increases, on the other hand the rounder shape of the pores improves the mechanical behavior.

Comparison of the microstructural characterization for the three UST conditions shows that 60 seconds of ultrasound is inadequate for semisolid processing. In contrast, 15 and 30 seconds of ultrasound resulted in

similar microstructural parameters that were suitable for thixoforming. Condition UST-30s, however, produced the smallest amount of entrapped liquid in the primary phase. This results in a slurry with improved rheological behavior because the presence of more free eutectic between the solid particles leads to better general material flow. Thus, for the rheological evaluation, only condition UST-30s was analyzed in the comparison with conditions MV and AC.

Table III. Microstructural Parameters After Partial Melting of Feedstock Produced Under Conditions AC, MV and UST for Al5Si5Zn Alloy in the Semisolid State (Average \pm Standard Deviation)

Processing Condition	Grain Size (μm)	Globule Size (μm)	Circularity	Porosity (Area Percent)
AC	155 \pm 24	104 \pm 27	0.59 \pm 0.22	3.3
MV	124 \pm 12	104 \pm 21	0.63 \pm 0.20	3.3
UST-15s	120 \pm 19	93 \pm 13	0.58 \pm 0.21	2.5
UST-30s	123 \pm 18	90 \pm 10	0.58 \pm 0.22	3.3
UST-60s	146 \pm 19	100 \pm 17	0.54 \pm 0.21	2.6

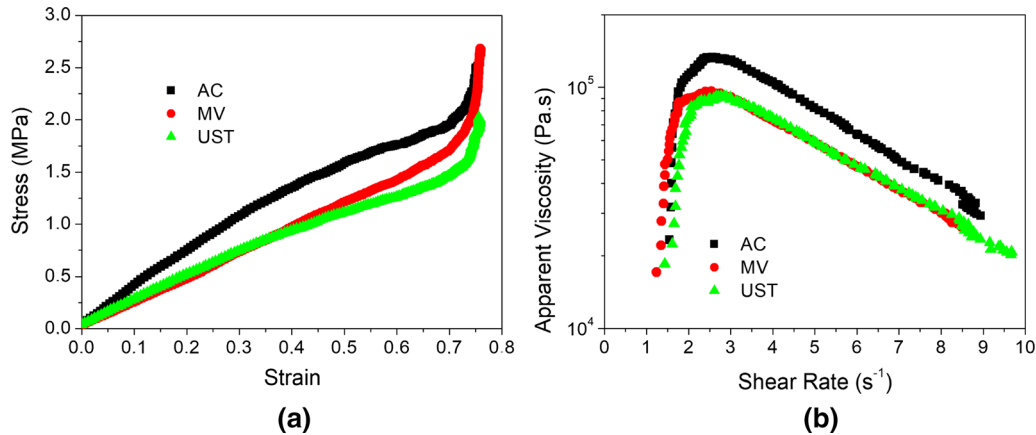


Fig. 4—Engineering stress vs strain (a) and apparent viscosity vs shear rate (b) curves for 0.45-solid-fraction Al5Si5Zn alloy during hot compression tests for conditions AC (black), MV (red) and UST-30s (green) (Color figure online).

Figure 4 shows the engineering stress vs strain (a) and apparent viscosity vs shear rate (b) curves for conditions AC (black curves), MV (red curves) and UST-30s (green curves) for hot compression of a 0.45-solid-fraction slurry of the Al5Si5Zn alloy.

In the engineering stress curves (Figure 4(a)), the stress increases as the deformation is imposed, reaching a maximum only at the end of the compression. This is because the semisolid slurry spreads rapidly, resulting in higher resistance to further deformation. The peak at the end of the test is due to cooling and progressive solidification of the sample in contact with the die, leading to forming in the solid state. Condition UST-30s has the smallest value of maximum stress, followed by conditions MV and AC. This result is associated with the microstructure of each condition and the correspondingly greater (UST-30s and MV) or lower (AC) flow ability.

Conditions MV and UST-30s have similar, lower values of maximum apparent viscosity than condition AC (Figure 4(b)). This behavior is associated with the smaller grain and globule sizes and higher circularity observed in the microstructural analysis for these two conditions, as a result of which these particles can flow more easily within the liquid. The coarse grains and smaller circularity observed for condition AC favor hooking between these particles, making them less mobile and resulting in slurries with higher viscosity.

The behavior of the viscosity is similar to that expected for semisolid slurries, *i.e.*, after the viscosity reaches a peak, the fragile connections between the solid particles break, destroying the 3D skeleton. The material then starts to flow easily, and the apparent viscosity decreases rapidly as the shear rate increases. At 9 s⁻¹ the viscosity is close to that of molten glass.^[1]

C. Characterization of the Thixoformed Part

Figure 5 shows OM images of the Al5Si5Zn alloy after open-die thixoforming for conditions AC (a to c), MV (d to f) and UST-30s (g, i). The images highlight, from left to right, respectively, grains, globules and precipitates, especially silicon particles.

Color metallography shows that all the conditions tested had many connections between the grains as a result of the large strain imposed during thixoforming. For the thixoforming described here, the larger the grains in the raw material, the larger the grains in the thixoformed part. In this case, the largest final grain size was observed for condition AC. Conventional B&W metallography shows that this condition resulted in a coarser structure while conditions MV and UST-30s produced a very globular, homogeneous morphology. In all the raw materials (AC, MV and UST), the silicon particles are coarser than those observed after heat treatment and thixoforming.

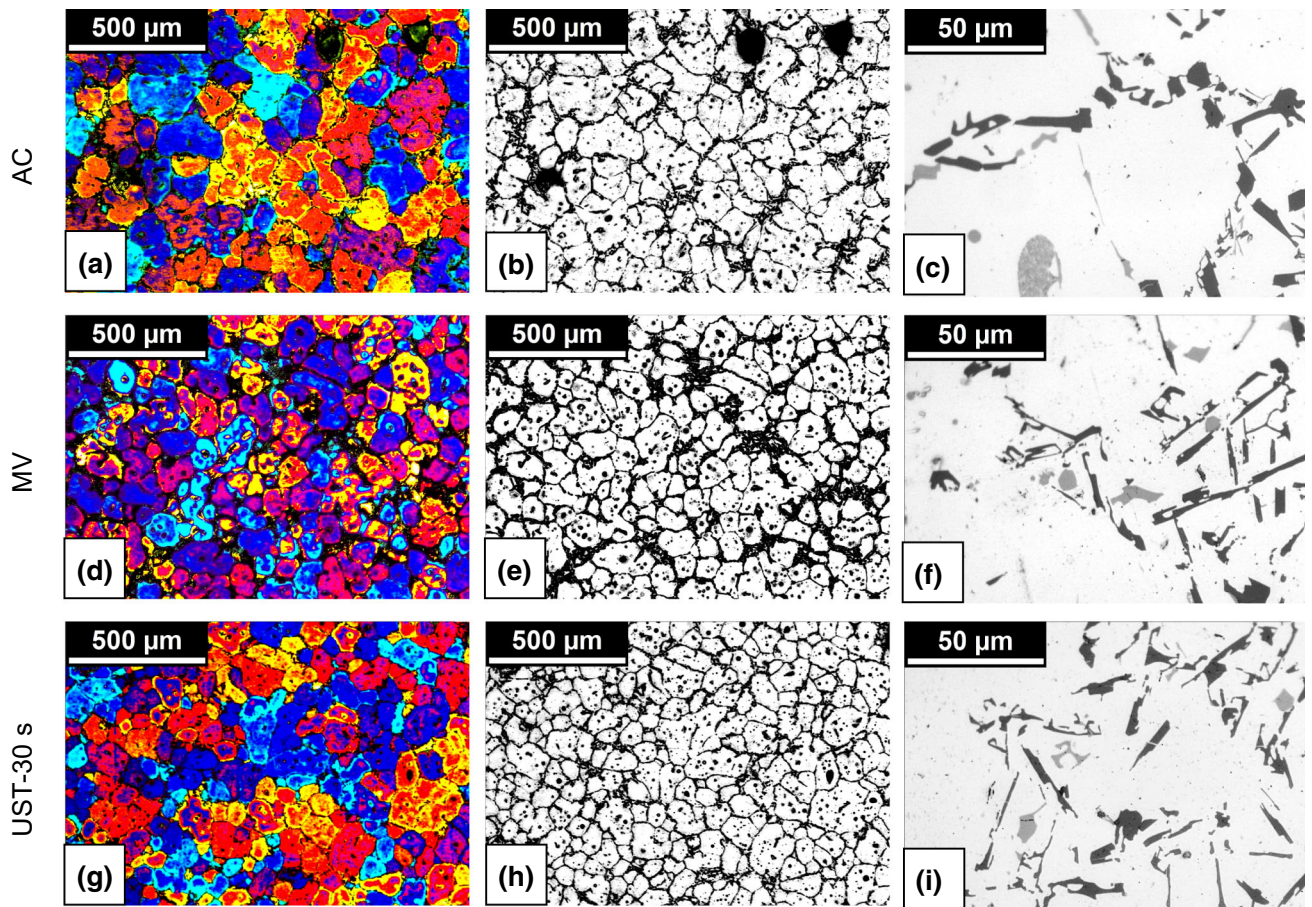


Fig. 5—OM images of the Al5Si5Zn alloy after open-die thixoforming following casting under conditions AC (a) through (c), MV (d) through (f) and UST-30s (g) through (i). The images on the left, in the middle and on the right highlight grains, globules and precipitates, respectively (Color figure online).

Comparative analysis of Figures 2, 3 and 5 shows that silicon particles are present in two distinct morphologies: particles with an acicular morphology, which are found at the edges of the primary phase and can act as a preferential locus for crack initiation, and circular clusters with thin crystals, which are found in the primary phase and, unlike the acicular crystals, can block dislocations and improve the mechanical behavior of the alloy. Even after compression, residual porosities (Figure 5—AC samples) with irregular shapes can be observed at the edge of the primary phase and constitute preferential crack-initiation sites.

Table IV shows the microstructural parameters of the thixoformed part for the three conditions tested, the average values of yield stress (σ_Y), ultimate tensile stress (σ_U) and strain (ϵ) obtained in tensile tests and the Vickers hardness.

Table IV shows that σ_Y , σ_U and HV are higher for smaller values of grain and globule size; this is expected as grain boundaries block dislocations and increase stress. In addition, smaller grains result in more widely distributed silicon crystals (with high hardness), making the average hardness rise. The highest σ_Y , σ_U and HV and most refined microstructures are observed for condition UST-30s. However, the differences between these results and the

corresponding results for the MV condition are not statistically significant. The similarity of tensile parameters in Table IV can be attributed to the homogeneous level of grain size, globule size as well as porosity present in all conditions. The effect of porosity probably prevailed over the small microstructural differences and affected the tensile results in a similar manner.

As expected, the forming process collapses the pores, making them smaller. The slightly higher residual porosity of the AC samples after thixoforming could partly explain the poorer mechanical behavior of the alloy produced under this condition. The smaller number of pores in the alloys produced under conditions MV and UST-30s may have helped to minimize/delay crack propagation and, therefore, resulted in higher values of stress and strain.

The difference in mechanical performance observed between the partially melted and thixoformed alloy can be explained by the breakdown of dendritic arms by shear and by the increase in circularity as a result of sintering during compression in the semisolid state. Furthermore, the thixoforged samples had half the porosity of the partially melted sample for each condition because of the collapse of pores during compression.

Table 4. Microstructural Parameters, Tensile Properties and Hardness After Thixoforming (Average \pm Standard Deviation)

Processing Condition	Grain Size (μm)	Globule Size (μm)	Porosity (Area Percent)	σ_Y (MPa)	σ_U (MPa)	ϵ (Pct)	HV
AC	150 ± 21	110 ± 13	1.15	107 ± 6.2	179 ± 8.8	4.3 ± 0.2	72.6 ± 1.6
MV	137 ± 19	100 ± 11	1.09	112 ± 1.0	189 ± 2.0	4.2 ± 0.4	78.6 ± 1.7
UST-30 s	124 ± 19	97 ± 11	1.08	117 ± 2.5	202 ± 7.5	5.5 ± 0.6	82.2 ± 3.6

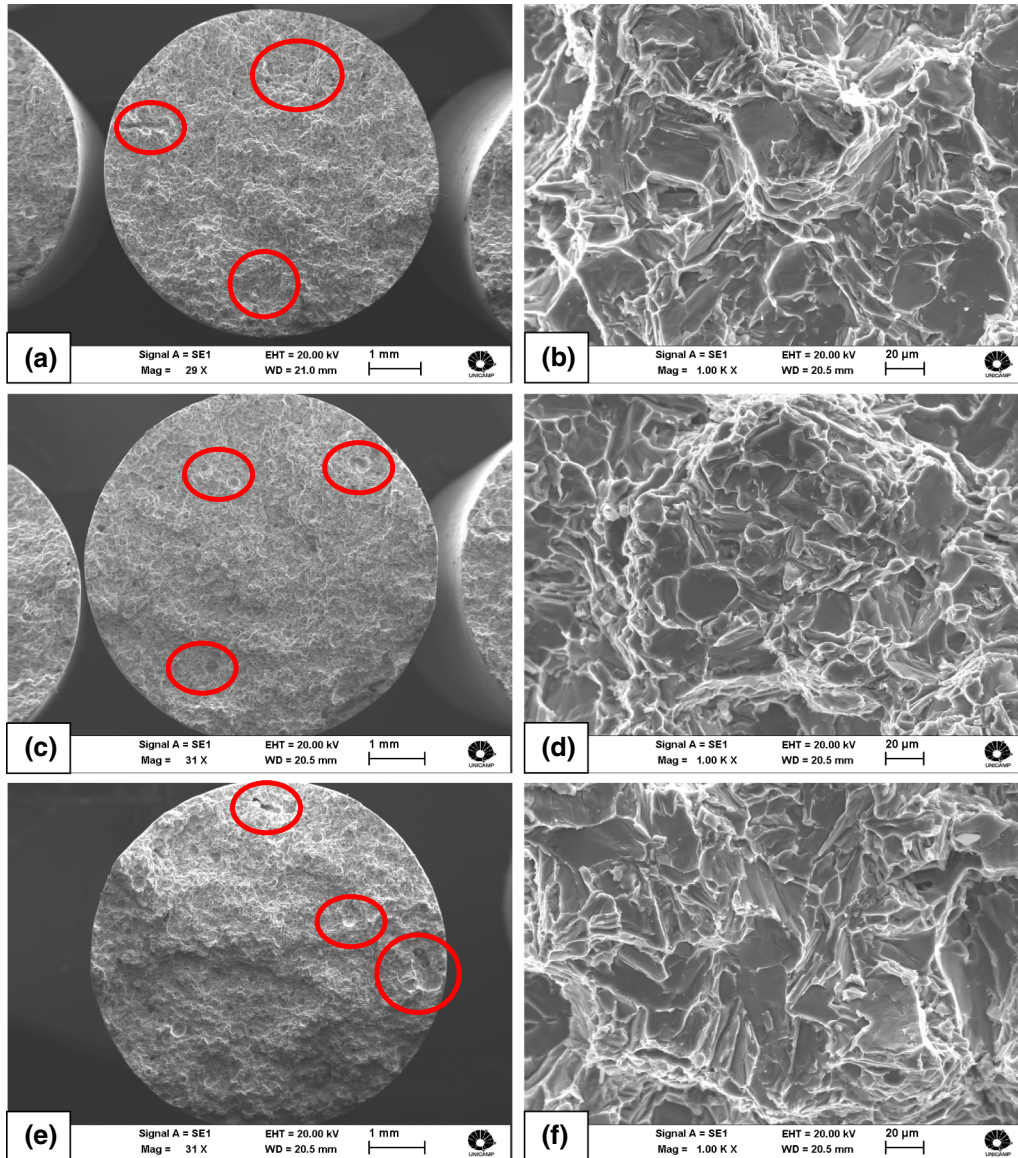


Fig. 6—SEM micrographs of the fracture surface of thixoformed parts produced using feedstock produced under conditions AC (a, b), MV (c, d) and UST-30s (e, f) (Color figure online).

Figure 6 shows SEM images of the fracture surface for conditions AC, MV and UST-30s. According to the ASM handbook, there are many microprecipitates that can adversely affect the mechanical behavior of aluminum alloys with a high silicon and zinc content in the presence of small amounts of Mg and Fe. Hence, considering the composition of the alloy, MgZn_2 and

Mg_2Si in the form of fine grains and coarser globules can be expected, as well as $\delta\text{-Al}_4\text{FeSi}_2$ platelets, FeAl_3 polygons, $\beta\text{-Al}_5\text{FeSi}$ needles and $\text{FeMg}_3\text{SiAl}_8$ in the form of Chinese script.^[24–26] Brittle Si-rich eutectic crystals are extensively present in the primary-phase grain boundary for all the tested conditions. These stress-concentrating precipitates are present in several

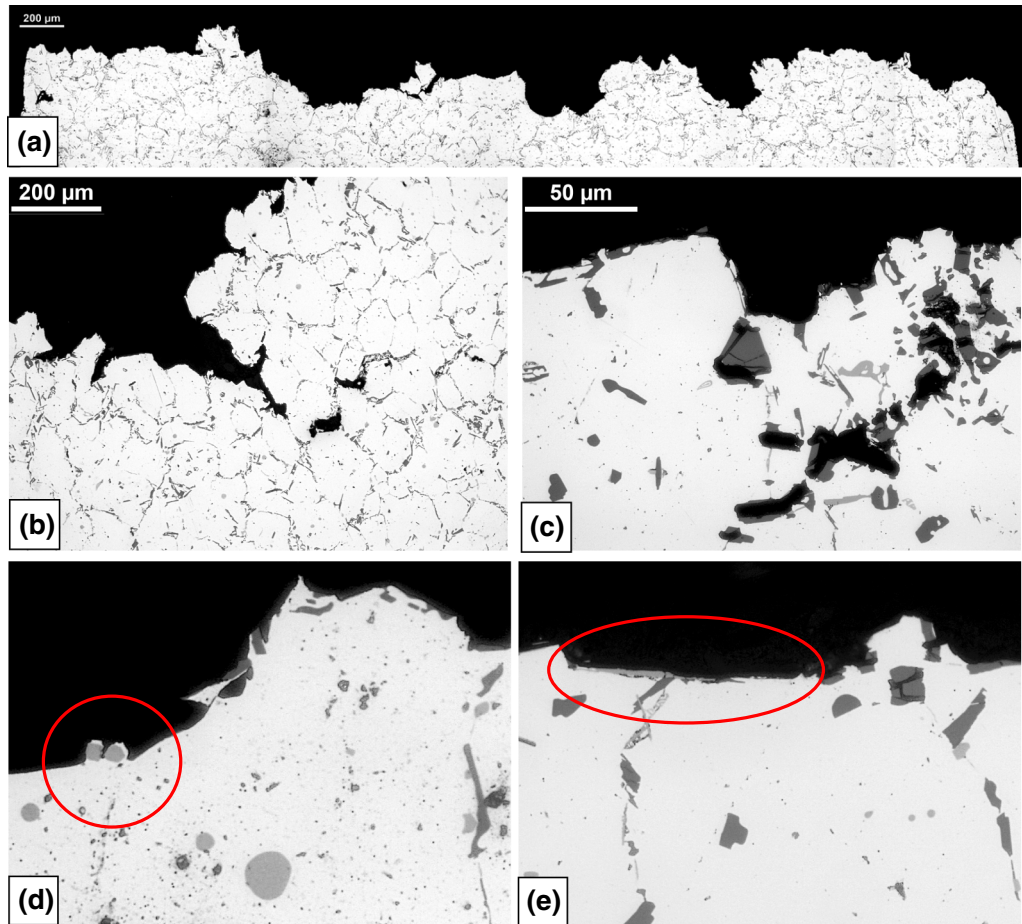


Fig. 7—Longitudinal section of the UST-30s sample in Fig. 6(a); zoom-in highlighting the intergranular fracture (b); a crack that has propagated along a region rich in Si particles (c); Fe precipitates at the fracture surface (d) and a region with a transgranular fracture favored by fragile particle clusters (e) (Color figure online).

regions of the fractured surface of the samples along with intergranular/cleavage facets, indicating the occurrence of fragile fracture. On the other hand, it can be seen that the primary phase also suffered a certain degree of plastic strain. Therefore, the fractured surface presents a hybrid fracture mode, predominantly fragile.

Figure 7 shows OM images highlighting a longitudinal section of the fractured region in Figure 6. The fracture presents a intergranular character, intensified by fragile eutectic particles (such as Si-rich and Fe-rich intermetallic) in the primary phase grain boundary (Figures 7(b), (d) and (f)). In Figures 6(a) through (c) and 7(d) and (e), pores and cracks in the Si crystals are highlighted in red. As these defects and particles break or undergo decohesion from the more ductile matrix, they propagate cracks. Figure 7(a) shows porosities in the fracture surface, another feature that probably favored intergranular fracture.

Fe-rich intermetallic (Figure 7(c) and (e)) can also be seen in the fracture region and probably act as preferential decohesion sites. The intergranular nature, planar aspect and low strain achieved before rupture (close to 4 pct) indicate that, in some small areas, the fracture is ductile. The slight curvature in the borders of the fractured sample (Figure 7(a)) indicates that discrete

necking occurred. However, this strain was not enough to cause severe plastic deformation of the grains, which show no visible deformation parallel to the direction of the stress (Figures 7(a) and (b)). Transgranular fracture (Figure 7(e)) adjacent to fragile particle clusters within the grain can also be observed, but in only a few regions. Both images 6 and 7 are then in agreement with the low elongation suffered by the tensile test samples (Table IV).

Finally, Figure 8 shows the surface of the sonotrode after it had been used for approximately 20 melts, *i.e.*, after around 10 kg of aluminum alloy had been processed. Cavitation has severely degraded the sonotrode, which had to be discarded. A similar degree of cavitation and low sonotrode life expectancy have been reported in several papers^[13,15,16] and can affect the viability of ultrasonic melt treatment prior to pouring. Our research group recently compared the effectiveness of titanium and AISI 4340 sonotrodes when used with 355 aluminum alloy and concluded that while they both have similar efficiency in terms of microstructural refinement and their use is limited by the same cavitation problem, the steel sonotrode had the advantage of being much cheaper.^[26] In this case, despite the elevated cost of the processing, the use of severe plastic deformation



Fig. 8—Image of the AISI 4340 sonotrode before and after it was used for UST (Color figure online).

such equal channel angular pressing and/or cold rolling could be a better solution for manufacturing raw material feedstock for semisolid processing.^[27,28]

IV. CONCLUSION

The results reported here show that the use of UST for 15, 30 and 60 seconds prior to casting of a 0.5 kg ingot was more effective in partially degassing the alloy than MV or AC. However, when the alloy was partially melted to 0.45 solid fraction in order to achieve the desired microstructure for thixoforming, further release and coalescence of retained gasses took place, annulling the advantage of the previous degassing associated with UST and resulting in similar porosity for all the casting conditions.

The use of UST for 15 and 30 seconds prior to casting resulted in the most refined and uniform microstructure, confirming the effectiveness of this pretreatment as a means of improving the microstructure of the alloy. However, after partial melting, the microstructural parameters were similar for the UST and MV samples, indicating that exposure in the semisolid state led to diffusion effects that eliminated the previous microstructural differences between the two casting conditions.

Consequently, both the UST and MV samples had similar rheological behavior during compression (open die thixoforming). The difference in apparent viscosity and engineering stress under compression between the two conditions was 3 and 16 pct, respectively. Condition AC resulted in microstructural and rheological parameters that were inferior to these obtained for conditions UST and MV.

Solid-particle shear and sintering were observed during thixoforming, leading to different distributions of silicon particles and other precipitates from those observed for the partially melted material. This resulted in improved mechanical performance (mechanical strength, ductility and hardness) for the MV and UST conditions. Condition UST resulted in slightly superior yield stress, ultimate tensile stress, total strain and

hardness to those for conditions MV and AC, but because the sonotrode was used directly in the melt, and therefore, had a low life expectancy, we strongly recommend mechanical vibration during solidification as a simple yet superior technique for use in the production of aluminum silicon alloy feedstock for semisolid processing.

ACKNOWLEDGMENTS

The authors would like to thank the Brazilian research funding agencies FAPESP (Fundação de Amparo à Pesquisa do Estado de São Paulo—Project 2015/22143-3), CNPq (Conselho Nacional de Desenvolvimento Científico e Tecnológico—PQ 304921/2017-3) and CAPES (Coordenação de Aperfeiçoamento de Pessoal de Nível Superior—Brasil (CAPES)—Finance Code 001) for providing financial support for this study. The authors are also indebted to the Faculty of Mechanical Engineering at the University of Campinas and Sonitron Ultra Sônica Ltda.

REFERENCES

1. M.C. Flemings: *Metall. Trans. A*, 1991, vol. 22A, pp. 957–81. <https://doi.org/10.1007/BF02661090>.
2. D.H. Kirkwood, M. Suéry, P. Kapranos, H.V. Atkinson and K.P. Young: *Semi-Solid Processing of Alloys*, Springer Series in Materials Science 124, Springer, Heidelberg, London, 2010, pp. 14–47. <https://doi.org/10.1007/978-3-642-00706-4>.
3. D. Liu, H.V. Atkinson, and H. Jones: *Acta Mater.*, 2005, vol. 53, pp. 3807–19. <https://doi.org/10.1016/j.actamat.2005.04.028>.
4. D. Zhang, H.V. Atkinson, H. Dong, and K. Zhu: *Metall. Mater. Trans. A*, 2017, vol. 48A, pp. 4701–12. <https://doi.org/10.1007/s11661-017-4235-2>.
5. E.J. Zoqui, D.M. Benati, C.T.W. Proni, and L.V. Torres: *Calphad*, 2016, vol. 52, pp. 98–109. <https://doi.org/10.1016/j.calphad.2015.12.006>.
6. G.L. Brollo, D.V. Tamayo, L.V. Torres, and E.J. Zoqui: *Calphad*, 2019, vol. 67, p. 101671. <https://doi.org/10.1016/j.calphad.2019.101671>.
7. D.H. Kirkwood: *Int. Mater. Rev.*, 1994, vols. 39–5, pp. 173–89. <https://doi.org/10.1179/imr.1994.39.5.173>.
8. V. Laxmanan and M.C. Flemings: *Metall. Trans. A*, 1980, vol. 11A, pp. 1927–37. <https://doi.org/10.1007/BF02655112>.
9. A. Ohno: *Solidification—The Separation Theory and its Practical Applications*, Springer-Verlag, Berlin Heidelberg, New York, 1987, pp. 15–57.
10. F. Taghavi, H. Saghafian, and Y.H.K. Kharrazi: *Mater. Des.*, 2009, vol. 30, pp. 1604–11. <https://doi.org/10.1016/j.matdes.2008.07.032>.
11. C.T.W. Proni, M.H. Robert, and E.J. Zoqui: *Arch. Mater. Sci. Eng.*, 2015, vol. 73, pp. 82–93.
12. G.I. Eskin: *Ultrasonic Treatment of Light Alloy Melts*, Gordon and Breach Science Publishers, Amsterdam, 1998, pp. 18–240.
13. T.V. Atamanenko, D.G. Eskin, L. Zhang, and L. Katgerman: *Metall. Mater. Trans. A*, 2010, vol. 41A, pp. 2056–66. <https://doi.org/10.1007/s11661-010-0232-4>.
14. Y.I. Frenkel: *Kinetic Theory of Liquid*, Dover Publications, New York, 1959, pp. 170–488.
15. G.I. Eskin: *Ultrason. Sonochem.*, 2001, vol. 8, pp. 319–25. [https://doi.org/10.1016/S1350-4177\(00\)00074-2](https://doi.org/10.1016/S1350-4177(00)00074-2).
16. Q. Han: *Metall. Mater. Trans. B*, 2015, vol. 46B, pp. 1603–14. <https://doi.org/10.1007/s11663-014-0266-x>.

17. C.T.W. Proni, L.C. de Paula, L.V. Torres, and E.J. Zoqui: *Solid State Phen.*, 2019, vol. 285, pp. 339–44. <https://doi.org/10.4028/www.scientific.net/SSP.285.339>.
18. C.T.W. Proni and E.J. Zoqui: *Int. J. Mater. Res.*, 2017, vol. 108, pp. 228–36. <https://doi.org/10.3139/146.111472>.
19. ASTM E8/E8M-16: *Standard Test Methods for Tension Testing of Metallic Materials*, ASTM International, West Conshohocken, PA, 2016. www.astm.org, https://doi.org/10.1520/e0008_e0008m-16a. Accessed 24 Mar 2016.
20. E.J. Zoqui, M.T. Shehata, M. Paes, V. Kao, and E. Es-Sadiqi: *Mater. Sci. Eng. A*, 2002, vol. 325, pp. 38–53. [https://doi.org/10.1016/s0921-5093\(01\)01401-0](https://doi.org/10.1016/s0921-5093(01)01401-0).
21. ASTM E112-13: *Standard Test Methods for Determining Average Grain Size*, ASTM International, West Conshohocken, PA, 2013. www.astm.org, <https://doi.org/10.1520/e0112-13>. Accessed 1 Aug 2018.
22. N.A. Baena, T. Pabel, N.V. Sierra, and D. Eskin: *Mater. Sci. Forum*, 2013, vol. 765, pp. 271–75. <https://doi.org/10.4028/www.scientific.net/MSF.765.271>.
23. L.C. de Paula and E.J. Zoqui: *SN Appl. Sci.*, 2019, vol. 1, pp. 394–409. <https://doi.org/10.1007/s42452-019-0399-2>.
24. ASM Handbook: *Metallography and Microstructures*, ASM Int., 2004. vol. IX. pp. 107–112. ISBN: 978-0-87170-706-2.
25. J.E. Hatch: *Aluminium: Properties and Physical Metallurgy*, American Society for Metals, Cleveland, 1984, pp. 154–424.
26. L. Zhang, D.G. Eskin, and L. Katgerman: *J. Mater. Sci.*, 2011, vol. 46, pp. 5252–5259. <https://doi.org/10.1007/s10853-011-5463-2>.
27. F. Czerwinski: *Metall. Mater. Trans. B*, 2018, vol. 49B (6), pp. 3220–57. <https://doi.org/10.1007/s11663-018-1387-4>.
28. K.N. Campo and E.J. Zoqui: *Metall. Mater. Trans. A*, 2016, vol. 47A (4), pp. 1792–1802. <https://doi.org/10.1007/s11661-016-3339-4>.

Publisher's Note Springer Nature remains neutral with regard to jurisdictional claims in published maps and institutional affiliations.